Superpixel-level CFAR Ship Detection Based on Polarimetric Bilateral Truncated Statistics

Wenxing Mu, Ning Wang, Lu Fang, and Tao Liu

***Abstract*—Constant false alarm rate (CFAR) detector is a common method for ship detection in polarimetric synthetic aperture radar (PolSAR) images. CFAR detectors greatly depend on the clutter modeling that can be easily affected by the contamination caused by both lower- and higher-intensity outliers, such as spilled oil and intensive targets. Traditional CFAR detectors perform detection in a pixel-by-pixel manner, which ignores the spatial information. Both the bias in clutter modeling and the absence of spatial information can degrade the ship target detection performance. In this study, a superpixel-level polarimetric bilateral truncated statistics CFAR detector is proposed to promote the ship target detection performance in complex ocean scenarios. As the preprocessing of the PolSAR image, the superpixel segmentation is conducted based on the multilook polarimetric whitening filter result to select candidate ship target superpixels for bilateral truncation and background clutter modeling. The elliptical truncation is expanded to a complex situation and the relationship between the second moments before and after truncation is derived. The maximum-likelihood estimation estimator of the equivalent number of looks based on the bilateral truncation distribution is derived and compared with other parameter estimators. The influence of the truncation depth on estimator performance is analyzed, according to which the adaptive bilateral truncation method is determined. The Gaussian mixture model and the Parzen window kernel method are compared with the model-based method and utilized for data fitting. The proposed method performs bilateral truncation based on the superpixel segmentation result to provide pure clutter samples for accurate parameter estimation and clutter distribution modeling, reducing time consumption and false alarms. The method is validated efficient on both simulated and measured data from RADARSAT-2.**

***Index Terms*—Bilateral truncated statistics (BTS), constant false alarm rate (CFAR), superpixel, synthetic aperture radar (SAR).**

I. Introduction

POLARIMETRIC synthetic aperture radar (PolSAR) is a widely applied remote sensing system that can provide multidimensional information regarding targets [1]. Among the fields, the PolSAR has been applied in ship target detection is significant. Among the detectors that have been proposed, the optimal polarimetric detector (OPD) based on the likelihood ratio test proposed by Novak et al. [2] performs well under the condition that the statistical distributions of the clutter and target are known. The polarimetric detection optimization filter can perform better than traditional detectors [3]. Different polarimetric detectors are combined in the joint polarimetric detector (JPD) by a modified LDA algorithm, which performs better than JPD [3]. The authors in [4] and [5] proposed the polarimetric whitening filter (PWF) to minimize the statistical variation caused by speckles and the PWF has been proven to share a comparable performance with the OPD. The multilook PWF (MPWF) proposed in [6] and [7] is an extension of the PWF. Liu et al. [8] derived the analytical expressions of the PFAs for different product models where the texture follows different distributions and the parameter estimators based on MPWF and log-cumulants were derived. The polarimetric notch filter (PNF) proposed in [9] and [10] performs well with minimum sea clutter power. Liu et al. [11] developed the PNF to a new form of the PNF (NPNF) by defining a new expression of power from the aspect of the physical mechanisms. Since the constraint of the bilateral truncation shares a similar form of the result of MPWF mathematically, the MPWF is used here for speckle reduction. The statistical model of the filter in nonhomogeneous sea clutter is developed for GP-PNF in [12]. In practice, it is difficult to obtain prior information about clutter and targets. Therefore, the constant false alarm rate (CFAR) detectors that do not require prior information were used [13]. The traditional cell-averaging CFAR (CA-CFAR) proposed in [14] performs the detection based on the average intensity of the pixels in the reference window. The greatest-of CFAR (GO-CFAR) [15] and the smallest-of CFAR (SO-CFAR) [16] both use spatial subsets to remove outliers. The variability CFAR (VI-CFAR) [17] adaptively selects reference pixels for background statistics modeling. The order statistic CFAR (OS-CFAR) [18] performs better when the clutter distribution and spatial division are complex. The trimmed mean CFAR (TM-CFAR) [19] is the generalization of the OS-CFAR.

In a CFAR detector, the accurate modeling of the background clutter is of great importance since the CFAR detector keeps the false alarm (PFA) constant by dynamically adjusting the detection threshold based on the background clutter modeling. Owing to the absence of prior information, parameter estimation, which requires pure clutter samples, is necessary for clutter modeling. Since the traditional CFAR detectors use the sliding window, the center of which is the pixel under test, to detect pixel by pixel, modeling deviation appears in complex ocean scenarios, such as spilled oil and intensive targets. The deviation is mainly caused by the contamination in clutter samples and the accurate

Manuscript received 24 August 2023; revised 15 November 2023 and 11 January 2024; accepted 17 January 2024. Date of publication 22 January 2024; date of current version 8 February 2024. This work was supported by the National Natural Science Foundation of China under Grant 62171452 and Grant 61771483. *(Corresponding author: Tao Liu.)*

The authors are with the School of Electronic Engineering, Naval University of Engineering, Wuhan 430033, China (e-mail: 739972725@qq.com; 236110031nn@sina.com; fangluflora@163.com; liutao1018@hotmail.com).

Digital Object Identifier 10.1109/JSTARS.2024.3356591

truncation is expected to eliminate outliers. Contamination can be caused by both higher- and lower-intensity outliers; therefore, the truncation is expected to be bilateral.

The CFAR detector based on truncated statistics (TS-CFAR) aiming at high-target-density situations has been applied in ship detection [20]. However, the method is implemented under the condition that the background sea clutter is homogeneous, which is not suitable for complex and changeable sea states. Although the improved segmentation-based CFAR detector using truncated statistics proposed in [21] solves the problem of target detection in nonhomogeneous situations, the truncation depth is artificially set and fixed which may lead to the over-truncation and the degradation of parameter estimation performance due to the reduction of sea clutter sample number. The truncation depth is studied in [22] and the quantile is applied to truncation for the CFAR detector based on the quantile truncated statistics. The above detectors are all aimed at the elimination of higher-intensity outliers. However, the clutter samples can also be contaminated by lower-intensity outliers. The CFAR detector based on bilateral truncation of log-normal distribution is proposed in [23]. The mentioned detectors utilizing truncated statistics are all based on first-order amplitude information. The detectors assume that the amplitude follows a certain distribution and deduce the estimation of parameters. When applied to PolSAR data, the detectors fail to utilize full polarimetric information. Although the PolSAR techniques enhance the targets in most ocean conditions, they cannot solve the deviation of clutter modeling caused by outliers. The relationship of second moments before and after unilateral truncation of multilook PolSAR data is derived in [24] and the PWF-TS-CFAR is proposed. The PWF-TS-CFAR detector determines the unilateral truncation threshold using an iterative method which is time-consuming. The PWF-TS-CFAR detector needs to be extended to bilateral truncation and an adaptive bilateral truncation method needs to be studied.

The concept of elliptical truncation was introduced into normal populations by Tallis, and the moment-generating function for the resulting distribution was derived in [25], which can be used to adjust the moments after truncation. The truncation proposed by Tallis is applied in the real 1-D situation. In this study, for utilizing full polarimetric information, the elliptical truncation is expanded to complex situations and combined with the MPWF which transforms the 9-D polarimetric information into 1-D result.

The parameter estimation in background clutter modeling is required since the prior information is out of reach. The estimation of ENL is of great importance in PolSAR image analysis and the equation derived from Tallis depends greatly on ENL. The maximum-likelihood estimation (MLE) estimator of the ENL utilizing the bilateral truncation distribution is derived in this study and compared with the estimators proposed in [26], [27], [28], [29], and [30]. The influence of the truncation depth on estimator performance is also analyzed and an adaptive bilateral truncation method is determined.

The pixel-by-pixel detecting manner also may bring more time consumption and false alarms owing to the lack of space information. To improve the performance in terms of time consumption and detection rate, a technique called superpixel segmentation in optical images was introduced into PolSAR image processing [31]. Simple linear iterative clustering (SLIC), a widely used superpixel segmentation method for optical images, was introduced into synthetic aperture radar (SAR) images in [30] and [32]. In this study, the superpixel segmentation is combined with MPWF to preprocess the PolSAR image. The pixels sharing similar MPWF intensity and located close to each other are clustered into the same superpixel, which ensures the strong correlation of space and intensity, for accurate bilateral truncation and modeling.

Compared with the conventional parametric model, the nonparametric model shows better performance in the probability density function (PDF) estimation. When applied in ship detection, the CFAR threshold must be solved from the PDF estimated by the nonparametric model. A numerical solution of the threshold of the Parzen window kernel method is given in [33]. The threshold is calculated by iterative interpolation of the complementary of cumulative distribution function (CDF) and its accuracy is limited by the number of samples, which may lead to the failure to meet the PFA accuracy requirements. The Morlet wavelet analysis and sparse theory are introduced to determine the Gaussian order number of the Gaussian mixture model (GMM) in [34]. The CFAR threshold is obtained by dichotomy. Although both GMM and Parzen window kernel methods are learning-based and have achieved better performance in PDF estimation, their performance in bilateral truncation cases has not been validated. In this article, the PDF estimation performance before and after bilateral truncation of GMM and the Parzen window kernel method is compared. The CFAR performance based on the learning-based and model-based methods in the bilateral truncation case is compared. According to the comparison, the methods are combined for accurate bilateral truncation threshold and CFAR threshold determination.

The main contributions and novelties of the superpixel-level polarimetric bilateral truncated statistics CFAR detector are as follows.

1) Based on the similarity between the expressions of the truncation constraint and MPWF, the elliptical truncation is expanded to a complex and multilook situation and combined with MPWF for calibrating the statistic distribution after bilateral truncation.
2) For taking the spatial information into consideration, superpixel segmentation is conducted based on the MPWF, which turns multidimensional complex polarimetric information into real data, to preprocess the PolSAR image and efficiently select candidate target superpixels in which the clutter shares strong correlation.
3) The MLE estimator of the ENL based on the gamma distribution after bilateral truncation is derived and compared with other estimators by simulated and real data.
4) The influence of the truncation depth on estimator performance is analyzed and the data fitting performance of GMM and Parzen window kernel method is compared. An adaptive bilateral truncation method is proposed.

The rest of this article is organized as follows. In Section II, we review the statistical PolSAR and MPWF data. Then, the bilateral truncation statistics is described. In Section III, the proposed superpixel-level polarimetric BTS

CFAR detector is described in detail. In Section IV, the simulated and measured data from RADARSAT-2 are used to validate the proposed method. Finally, Section V concludes this article.

II. Statistical Model

A. Description of PolSAR Data

The full polarimetric information of a single target is described by the Sinclair matrix, using linear horizontal and vertical polarization bases [1], as follows:

$$\mathbf{S} = \begin{bmatrix} S_{\mathrm{HH}} & S_{\mathrm{HV}} \\ S_{\mathrm{VH}} & S_{\mathrm{VV}} \end{bmatrix}. \tag{1}$$

The vectorization of $\mathbf{S}$ can be defined as in the following equation when $S_{\mathrm{HV}} = S_{\mathrm{VH}}$ is satisfied under the reciprocal condition:

$$\mathbf{k} = \begin{bmatrix} S_{\mathrm{HH}} & \sqrt{2}S_{\mathrm{HV}} & S_{\mathrm{VV}} \end{bmatrix}' \tag{2}$$

where $'$ is the transpose operator and coefficient $\sqrt{2}$ preserves total power of the signal.

Multilook processing is performed to reduce the number of speckles in the SAR images. The covariance matrix can be obtained as follows [4], [7]:

$$\mathbf{C} = \frac{1}{L}\sum_{i=1}^{L} \mathbf{k}_i \mathbf{k}_i^{\dagger} \tag{3}$$

where the superscript † denotes conjugate transpose.

As a random variable, the multilook covariance matrix $\mathbf{C}$ follows a Wishart distribution when $\mathbf{k}$ follows a Gaussian distribution and its PDF is [40], [41]

$$f_C(\mathbf{C}) = \frac{L^{Ld}|\mathbf{C}|^{L-d}\exp(-L\mathrm{tr}(\mathbf{\Sigma^{-1}C}))}{\Gamma_d(L)|\mathbf{\Sigma}|^{L}} \tag{4}$$

where L is the number of looks, d is the dimension of $\mathbf{C}$, and $\mathbf{\Sigma} = \mathrm{E}\{\mathbf{C}\}$ is the statistical mean (SM) of the multilook covariance matrix $\mathbf{C}$. $\mathrm{E}\{\boldsymbol{.}\}$ and $\mathrm{tr}(\boldsymbol{.})$ represent the expectation operator and trace operator, respectively. $\Gamma_d(L)$ is

$$\Gamma_d(L) = \pi^{\frac{1}{2}d(d-1)}\Gamma(L)\ldots\Gamma(L-d+1)\ldots \tag{5}$$

where $\Gamma(a) = \int_0^{\infty} y^{a-1}e^{-y}dy$ is the gamma function.

B. MPWF

The PWF proposed by Novak and Burl reduces the speckle via fully PolSAR data. The enhancement of target detection performance by PWF is proved in [35] and Liu et al. [7] extended the PWF to MPWF to generate a minimum-speckle intensity image by processing the multilook covariance matrix.

The MPWF for L looks can be obtained from [4]

$$z = \frac{1}{L}\sum_{i=1}^{L} \mathbf{k}_i^{\dagger}\mathbf{\Sigma}^{-1}\mathbf{k}_i = \mathrm{tr}\left(\mathbf{\Sigma}^{-1}\mathbf{C}\right) \tag{6}$$

where z follows a gamma distribution with the Gaussian assumption [24], [36].

$$z \sim \gamma\left(Ld, \frac{1}{L}\right). \tag{7}$$

Its CDF is

$$F_z(z; L, d) = \Gamma\left(Ld, Lz\right) \tag{8}$$

where $\gamma(\alpha, \beta)$ represents the Gamma distribution and can be represented as follows [28], [42]:

$$\gamma(\alpha, \beta) = \frac{1}{\Gamma(\alpha)}\frac{1}{\beta}\left(\frac{x}{\beta}\right)^{\alpha-1}\exp\left(-\frac{x}{\beta}\right) \tag{9}$$

where α is the shape parameter and β is the scale parameter.

C. Bilateral Truncated Statistics

Both lower- and higher-intensity outliers affect the modeling of clutter greatly such that the parameter estimation can be inaccurate, which causes poor detection performance. In this study, outliers are eliminated using bilateral truncation to create an accurate statistical model.

The PDF of truncated statistics can be expressed as follows:

$$\begin{aligned} f_{\tilde{z}}(z; \rho_1, \rho_2) &= f_z\left(z \,|\rho_1 \le z \le \rho_2\right) \\ &= \begin{cases} \frac{f_z(z)}{F_z(\rho_2) - F_z(\rho_1)}, & \rho_1 \le z \le \rho_2 \\ 0, & \text{else} \end{cases} \end{aligned} \tag{10}$$

where $f_z(z)$ and $F_z(z)$ are the PDF and CDF of the untruncated data z, respectively, and $\tilde{z}$ denotes the bilateral truncated data of z with a lower truncating-threshold ρ_1 and higher truncating-threshold ρ_2.

Tallis [25] derived an equation between the moments before and after elliptical truncation in normal populations. The truncation constraint is set to

$$E = \left\{\mathbf{x} | a \le \mathbf{x}'\mathbf{R}^{-1}\mathbf{x} \le b\right\}, 0 \le a < b \tag{11}$$

where $'$ is the transpose operator and $\mathbf{x}$ is an n-dimension multinormal vector. The equation for the moments before and after truncation is derived as follows:

$$\mathbf{M} = \alpha^{-1}\left[F_{n+2}(b) - F_{n+2}(a)\right]\mathbf{R} \tag{12}$$

where $\alpha = F_n(b) - F_n(a)$ and $F_{n+2i}(\boldsymbol{.})$ represent the chi-square distribution function with the parameter $n + 2i$. $\mathbf{M}$ is the moment of the truncated data.

Combined with the expression of the MPWF and the relationship between the chi-square distribution function $F_n(\boldsymbol{.})$ and incomplete gamma function $\Gamma(a, b)$, the real number results reported in [25] can be extended to the complex and multilook case (see Appendix), which is stated as follows:

$$\begin{aligned} \mathbf{\Sigma} &= \mu\left(\rho_1, \rho_2\right)\mathfrak{S}\left(\rho_1, \rho_2; \mathbf{\Sigma}\right) \\ \mu\left(\rho_1, \rho_2\right) &\equiv \frac{\Gamma\left(Ld, L\rho_2\right) - \Gamma\left(Ld, L\rho_1\right)}{\Gamma\left(Ld+1, L\rho_2\right) - \Gamma\left(Ld+1, L\rho_2\right)} \end{aligned} \tag{13}$$

with $\Gamma(a, b) = \frac{1}{\Gamma(a)}\int_0^b y^{a-1}e^{-y}dy$.

Substituting (13) into (6), we find that the distribution of the truncated data without calibration is expressed as follows:

$$z \sim \gamma\left(Ld, \frac{\mu(\rho_1, \rho_2)}{L}\right). \tag{14}$$

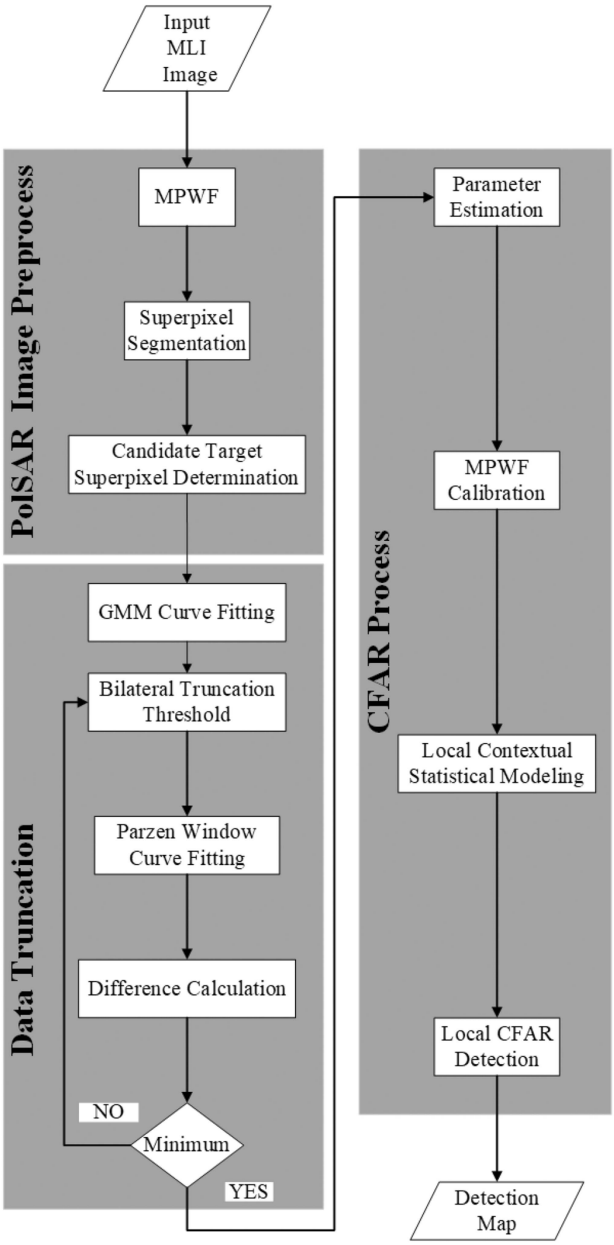

Fig. 1. Workflow of superpixel-level BTS CFAR detector.

For simplification, we denote $\mu = \mu(\rho_1, \rho_2)$. The PDF of truncated data $\tilde{z}$ can be written as follows:

$$f_{\tilde{z}}(z; L, d) = \begin{cases} \left(\frac{L}{\mu}\right)^{Ld} \frac{z^{Ld-1}\exp\left(-\frac{Lz}{\mu}\right)}{\Gamma(Ld)\left[\Gamma\left(Ld, \frac{L\rho_2}{\mu}\right) - \Gamma\left(Ld, \frac{L\rho_1}{\mu}\right)\right]}, & \rho_2 \le z \le \rho_2 \\ 0, & \text{else} \end{cases}. \quad (15)$$

III. Superpixel-Level Polarimetric Bilateral Truncated Statistics CFAR Detector

The workflow of the proposed superpixel-level polarimetric BTS CFAR detector is shown in Fig. 1. The operation of the superpixel-level BTS CFAR detector can be divided into PolSAR image preprocessing, data truncation, and CFAR processing as described in this section at length.

A. PolSAR Image Preprocess

The 3-D polarimetric covariance matrix is transformed to 1-D via MPWF presented as (6) and used for SLIC superpixel segmentation, and the distance can be defined as D given as

$$\begin{aligned} D &= \sqrt{d_c^2 + \left(\frac{d_s}{N_s}\right)^2 m^2} \\ d_c &= \sqrt{(I_i - I_j)^2} \\ d_s &= \sqrt{(x_i - x_j)^2 + (y_i - y_j)^2} \end{aligned} \quad (16)$$

where the subscripts i and j represent different pixels, $[x, y]$ is the position of the pixel, and the MPWF value is I. m is the compactness coefficient representing the weight between intensity distance and space distance. m is a coefficient adjusting the weight between the spatial and intensity information. We set $m = 2$ in our experiment. N_s is the expected superpixel number and should be set in accordance with the target size [37]. It can be calculated by the formula as follows:

$$N_s = \frac{M_1 \cdot M_2}{k \cdot A_{\max}} \quad (17)$$

where $A_{\max}$ is the area of the largest target and k is a coefficient which is positive. We set $k = 1.5$ in our experiment. The candidate target superpixels are selected using the threshold obtained from the average MPWF value of a pure clutter region. The threshold is set to be the mean MPWF value of a pure clutter region, denoted as Th. For every superpixel SP_i, the mean MPWF value of all the pixels it contains is calculated, denoted as AVE_i. If AVE_i is larger than Th, then the superpixel SP_i is selected as target superpixel.

B. Data Truncation

The truncation threshold greatly determines whether the outliers can be eliminated completely. We need to set the truncation thresholds suitably and adaptively. Due to the contamination, the untruncated data cannot be accurately fitted with a certain model. Therefore, we utilized GMM for fitting to accurately find the local minimums of the PDF and determine the iteration starting point of the truncation threshold. The PDF of the candidate target superpixels is estimated by GMM which is described as follows:

$$p(z|\boldsymbol{\Theta}) = \sum_{m=1}^{M} \omega_m N\left(z|\boldsymbol{\theta}_m\right) \quad (18)$$

where $N(z|\boldsymbol{\theta}_m)$ represents the single component of the mixture and ω_m is the weight of the component. M is the number of Gaussian functions. $\boldsymbol{\Theta} = [\boldsymbol{\theta}_1, \boldsymbol{\theta}_2, \ldots\ldots, \boldsymbol{\theta}_M]$ denotes the parameter vector for each component, where $\boldsymbol{\theta}_m = [\mu_m, \sigma_m, \omega_m]$. μ_m and σ_m are the mean and standard deviation of the Gaussian probability function, respectively. The PDF should be trimodal as shown in Fig. 2(a).

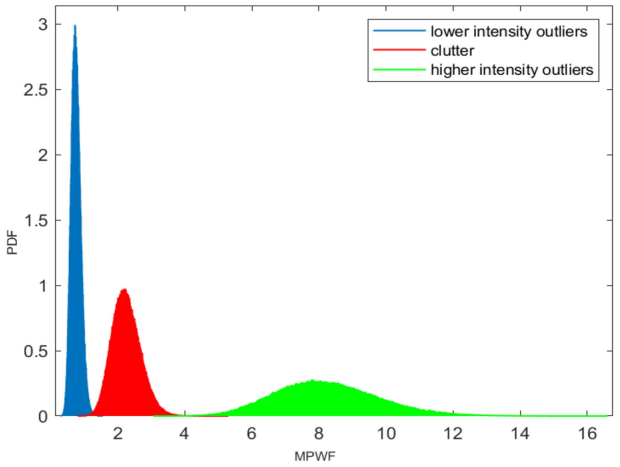

(a)

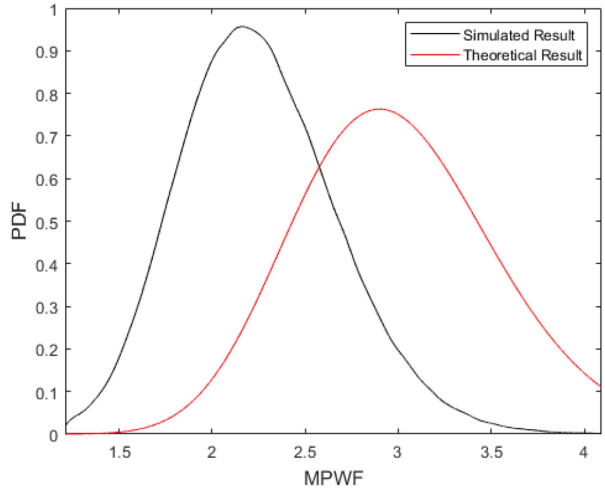

(b)

Fig. 2. Validation of truncated statistics. (a) Simulated data. (b) Truncated data.

However, due to the influence of sample size and amplitude, it is difficult to clearly observe three peaks in the PDF in some detected regions although the outliers exactly exist. Thus, the truncation threshold here is determined in a traversal manner.

The max value of the PDF is found and the corresponding MPWF value is denoted as x_{MAX}. The first PDF local minimum value of which the corresponding MPWF value is smaller than x_{MAX} is found and the MPWF value is defined as x_1. The second local minimum value of which the corresponding MPWF value is larger than x_{MAX} is found and the MPWF value is defined as x_2. The lower- and higher-truncation thresholds are, respectively, set as ρ_1 and ρ_2, where $\rho_1 \in [x_1, x_{\mathrm{MAX}}]$ and $\rho_2 \in [x_{\mathrm{MAX}}, x_2]$.

Second, the Parzen window kernel method is used to fit a curve Y_{PDF} for the PDF of the truncated data $\tilde{z}$. The Parzen window kernel method actually models the PDF with the accumulation of different kernel functions as follows:

$$Y_{\mathrm{PDF}} = \frac{1}{N}\sum_{j=1}^{M}\frac{1}{h_N}\varphi\left(\frac{\tilde{z}-\tilde{z}_j}{h_N}\right) \tag{19}$$

where $\varphi(u) = \frac{1}{\sqrt{2\pi}}\exp(-\frac{u^2}{2})$ and $\tilde{z}_1, \tilde{z}_2, \ldots\ldots, \tilde{z}_N$ denote the truncated data samples. N is the number of truncated samples. The width of the kernel function is $h_N = \frac{h}{\sqrt{N}}$ and h is set as 40 here. Then, the mean value and variance of the truncated data $\tilde{z}$ are calculated for the theoretical gamma distribution Y_{GT} as

$$Y_{\mathrm{GT}} = \frac{1}{\Gamma(\alpha)}\frac{1}{\beta}\left(\frac{\tilde{z}}{\beta}\right)^{\alpha-1}\exp\left(-\frac{\tilde{z}}{\beta}\right) \tag{20}$$

where

$\alpha = \frac{\mathrm{mean}(\tilde{z})^2}{\mathrm{var}(\tilde{z})}$ and $\beta = \frac{\mathrm{var}(\tilde{z})}{\mathrm{mean}(\tilde{z})}$.

The difference between the theoretical gamma distribution and the PDF of the truncated data is defined as Δ given as

$$\Delta = \frac{N_T}{N_A}\sum|Y_{\mathrm{GT}} - Y_{\mathrm{PDF}}| \tag{21}$$

where N_T is the number of the truncated data and N_A is the number of the data before truncation.

Finally, the minimum of the difference Δ is found and the corresponding truncation threshold ρ_1 and ρ_2 are selected.

C. CFAR Process

According to (13), $\mu(\rho_1, \rho_2)$ depends only on the number of looks when the bilateral truncation threshold is set. Typically, the number of looks is substituted by the ENL, which describes the averaging degree of the measured data and can be a noninteger. The MLE of the ENL is derived as

$$\begin{aligned}\mathcal{L}(L\,|\tilde{z}) &= \prod_{i=1}^{n} f_{\tilde{z}}(\tilde{z}_i\,|L) \\ &= (L)^{nLd}\frac{\exp(-L\sum_{i=1}^{n}\tilde{z}_i)}{\Gamma(Ld)^n[\Gamma(Ld, L\rho_2)-\Gamma(Ld, L\rho_1)]^n}\prod_{i=1}^{n}\tilde{z}_i^{Ld-1}\end{aligned} \tag{22}$$

where $\{\tilde{z}_i\}_{i=1}^{n}$ represents the truncated MPWF outputs with sample size n.

The log-likelihood function is derived as follows:

$$\begin{aligned}\log\mathcal{L}(L\,|\tilde{z}) &= nLd\log L - n\log\Gamma(Ld, L\rho_2) - \Gamma(Ld, L\rho_1) \\ &\quad -n\log\Gamma(Ld) - nL\frac{1}{n}\sum_{i=1}^{n}\tilde{z}_i + n(Ld-1)\frac{1}{n}\sum_{i=1}^{n}\log(\tilde{z}_i)\end{aligned} \tag{23}$$

where $(1/n)\sum_{i=1}^{n}\tilde{z}_i$ and $(1/n)\sum_{i=1}^{n}\log(\tilde{z}_i)$ are the SMs of the truncated and logarithmic-truncated data, respectively. Thus, we can obtain the MLE estimate of the ENL as follows:

$$\widehat{L} \subseteq \arg\max_{L}\{\log L(L\,|\tilde{z})\}. \tag{24}$$

ENL can also be estimated using other methods, such as those reported in [26], [27], [28], [29], and [30]. The ENL is estimated as a constant for the whole image and the MPWF data is adjusted by (7) and (14). The CFAR detection is performed for every target superpixel. The specified false alarm rate P_{FA} is defined as follows:

$$P_{\mathrm{FA}} = 1 - F_z(T; \widehat{L}, d) = 1 - \Gamma\left(\widehat{L}d, \widehat{L}T\right). \tag{25}$$

The detection threshold T can be obtained from

$$T = \frac{1}{\widehat{L}}\Gamma^{-1}\left(\widehat{L}d, 1 - P_{\text{FA}}\right) \tag{26}$$

where $\widehat{L}$ is the estimated ENL.

IV. Experiments and Validation

A. Simulated Data

The total simulation sample size is set as $N = [1000\ \ 5000\ \ 10\,000\ \ 50\,000\ \ 100\,000\ \ 500\,000]$. R_{c1} and R_{c2} are, respectively, defined as the contaminated proportion of the lower and higher intensity. Then, $N_c = N \cdot (1 - R_{c1} - R_{c2})$ bootstrap samples are drawn from the synthetic covariance matrices colored by $\mathbf{\Sigma}_C$ as the simulated clutter data. $N_1 = N \cdot R_{c1}$ samples are drawn from the synthetic covariance matrices colored by $\mathbf{\Sigma}_L$ as the simulated data for lower-intensity outliers. $N_2 = N \cdot R_{c2}$ samples are drawn from the synthetic covariance matrices colored by $\mathbf{\Sigma}_H$ as the simulated data for higher-intensity outliers. $\mathbf{\Sigma}_C$, $\mathbf{\Sigma}_L$, and $\mathbf{\Sigma}_H$ are all polarimetric covariance matrices drawn from RADARST-2 by the method of ensemble average of the selected regions representing sea clutter, lower- and higher-intensity outliers. The lower outliers to clutter ratio or higher outliers to clutter ratio can be defined as $\text{TCR}_i = \text{tr}(\mathbf{\Sigma}_i - \mathbf{\Sigma}_C)/\text{tr}(\mathbf{\Sigma}_C)$, $i = L$ or H. We set $R_{c1} = 0.3$, $R_{c2} = 0.2$, $\text{TCR}_1 = 2$, and $\text{TCR}_2 = 0.5$ here. R_{t1} and R_{t2} are defined as the truncating depth of the lower and higher intensity, respectively.

The correctness of the truncated distribution derived in (15) can be validated with the simulated data. The simulated data with the size of $N = 50\,000$ is shown in Fig. 2(a). In Fig. 2(b), the distribution after accurate truncation is represented by a black curve, and the theoretical PDF for (15) is depicted by a red curve. The difference between (7) and (14) is the coefficient $\mu(\rho_1, \rho_2)$ and it can be validated in Fig. 2(b) that the distribution of the simulated data is offset to the left compared to the theoretical one centered at 3.

B. Comparison of Data Fitting

The data fitting performance of GMM and Parzen window kernel method of the untruncated and truncated data is compared by 1000 Monte Carlo simulations with the sample size of $N = [1000\ \ 5000\ \ 10\,000\ \ 50\,000\ \ 100\,000\ \ 500\,000]$. The performance is assessed by the KL distance defined as

$$\begin{aligned} D_{\text{KL}} &= D(q||p) + D(p||q) \\ D(q||p) &= \sum q(\omega)\ \triangle\ \omega \cdot \log_2\left(\frac{q(\omega)\ \triangle\ \omega}{p(\omega)\ \triangle\ \omega}\right) \\ &= \sum Q(\omega) \cdot \log_2\left(\frac{Q(\omega)}{P(\omega)}\right) \end{aligned} \tag{27}$$

where $p(\omega)$ and $q(\omega)$ denote the theoretical and actual PDF, respectively. $P(\omega)$ and $Q(\omega)$ are the values of probability.

From the KL distance shown in Fig. 3(a) and (b), observe that GMM performs better when the data is untruncated, whereas

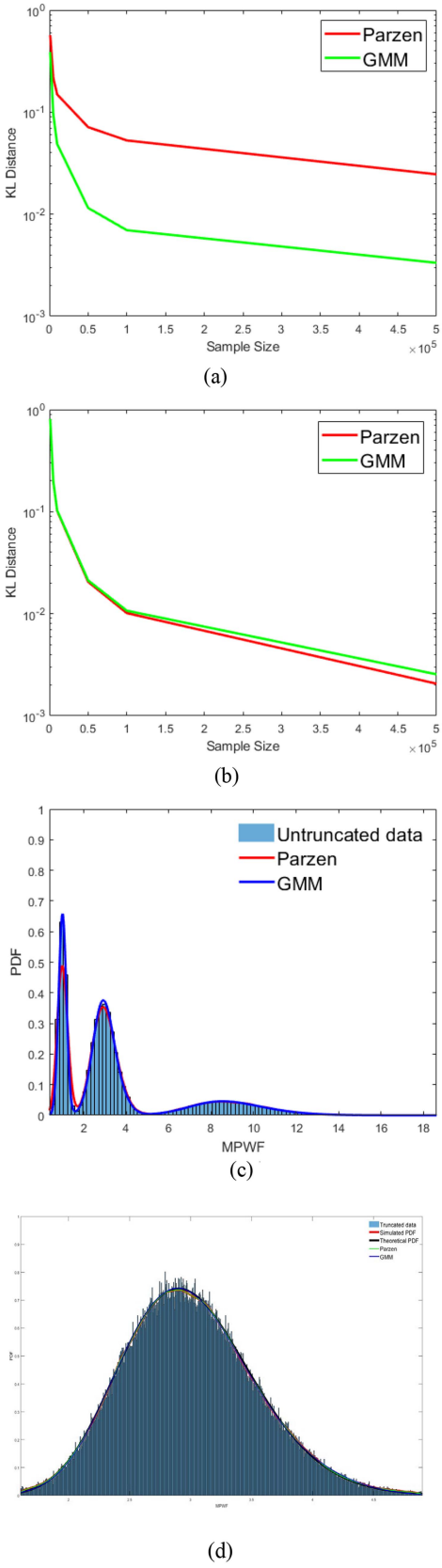

Fig. 3. Data fitting performance. (a) KL distance (untruncated data). (b) KL distance (truncated data). (c) Histogram and PDF (untruncated data). (d) Histogram and PDF (truncated data).

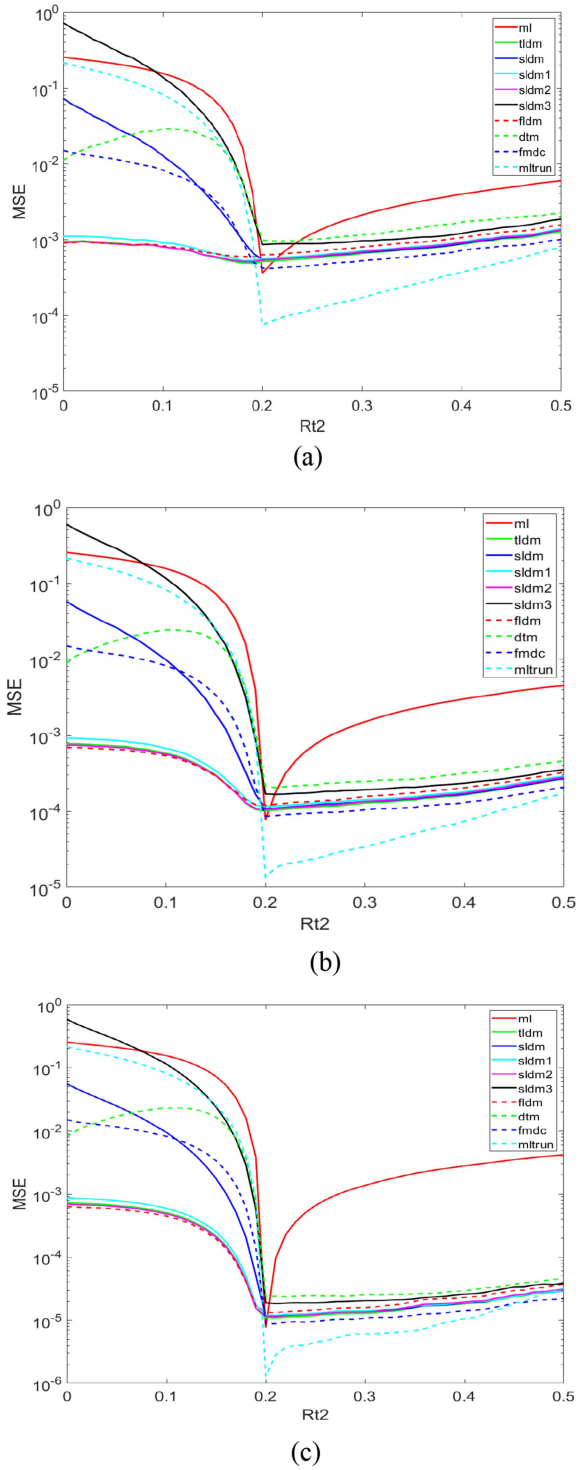

Fig. 4. Parameter estimation performance $R_{t1} = 0.2$. (a) 1000 samples. (b) 5000 samples. (c) 50 000 samples.

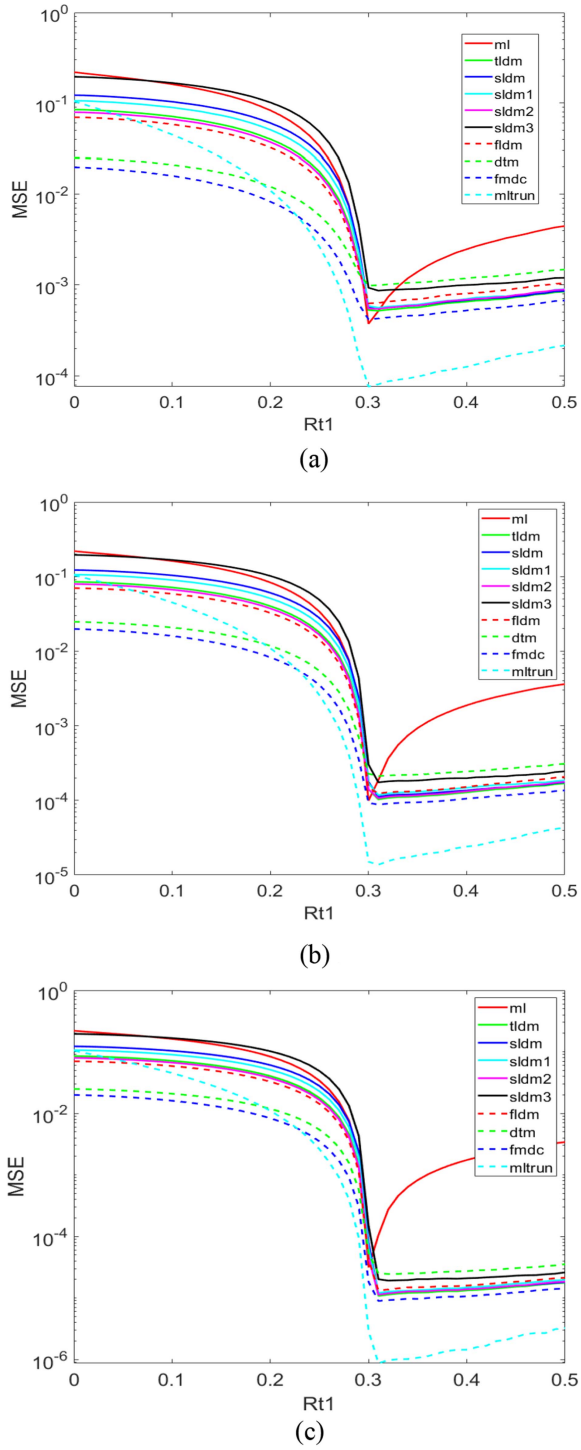

Fig. 5. Parameter estimation performance $R_{t2} = 0.3$. (a) 1000 samples. (b) 5000 samples. (c) 50 000 samples.

the Parzen window kernel method fits the truncated data better. It is also obvious that both GMM and Parzen window kernel method are greatly affected by the sample size. The reduction of the sample size can cause a great degeneration of the fitting performance. The histogram and PDF of the untruncated and truncated data of 500 000 samples are presented in Fig. 3(c) and (d), respectively.

C. Comparison of ENL Estimators

The comparison of the ENL estimators is performed via 1000 Monte Carlo simulations. The performance of the estimators under different truncation conditions is compared and the influence of truncation depth on estimation is analyzed. The performance of different ENL estimators is assessed using the mean square

error (MSE) metric [24], which is defined as

$$\begin{aligned}\text{Bias}(\widehat{L}) &= \left|\text{E}(\widehat{L}) - L\right|/L \\ \text{Var}(\widehat{L}) &= \text{E}\left\{\left[\text{E}(\widehat{L}) - \widehat{L}\right]^2\right\}/L^2 \\ \text{MSE}(\widehat{L}) &= \text{E}\left[(\widehat{L} - L)^2\right]/L^2 = \text{Bias}(\widehat{L})^2 + \text{Var}(\widehat{L}) \end{aligned} \quad (28)$$

where L is the true value and $\widehat{L}$ is the estimation of ENL.

The results in the case of the accurate truncation of the lower outliers are listed in Fig. 4. The results for accurate truncation of the higher outliers are listed in Fig. 5.

In both Figs. 4 and 5, the sldm, sldm1, sldm2, sldm3, fldm, and tldm estimators are based on the submatrices expressed in [28], which are denoted as ENL-SM. The dtm estimator, denoted as ENL-DTM, is based on the trace moments reported in [27]. The ml estimator is proposed in [26] and we use it as ENL-ML. The fmdc estimator based on the fractional determinant moments is proposed in [29], denoted as ENL-FMDC. The mltrun estimator is proposed in this study for BTS, which can be solved using (18) and is denoted as ENL-MLT.

From the results depicted in Figs. 4 and 5, observe that ENL-ML performs well only when the truncation is accurate. The ENL-SM, ENL-FMDC, and ENL-DTM estimators performed similarly when outliers are eliminated completely. However, sldm1, sldm2, sldm3, fldm, and tldm estimators performed better when higher-intensity outliers are incompletely eliminated. The ENL-MLT estimator provides the best performance under over-truncation.

Observe the performance of the ENL-SM, ENL-FMDC, ENL-DTM, and ENL-MLT under the condition that the lower- and higher-intensity outliers are eliminated completely, it can be found that the increase of the truncation depth has little effect on the performance of the estimators, which indicates that over-truncation is acceptable.

D. CFAR Performance

The performance of CFAR detectors is assessed by the false alarm rate maintenance C_L and the detection rate P_d as follows:

$$C_L = 10\log\left(\frac{P_{\text{fa}}}{P_{\text{FA}}}\right) \quad (29)$$

where P_{FA} is denoted as the specified false alarm rate and P_{fa} can be calculated from

$$P_{\text{fa}} = \frac{n_{\text{fa}}}{n} \quad (30)$$

where n_{fa} is the number of false alarms and n is the total number of samples.

The detection rate is measured as

$$P_d = \frac{n_d}{n_t} \quad (31)$$

where n_d is the number of the detected targets and n_t is the total number of targets.

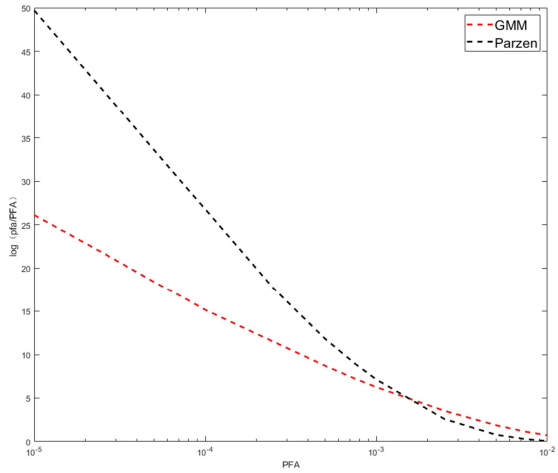

(a)

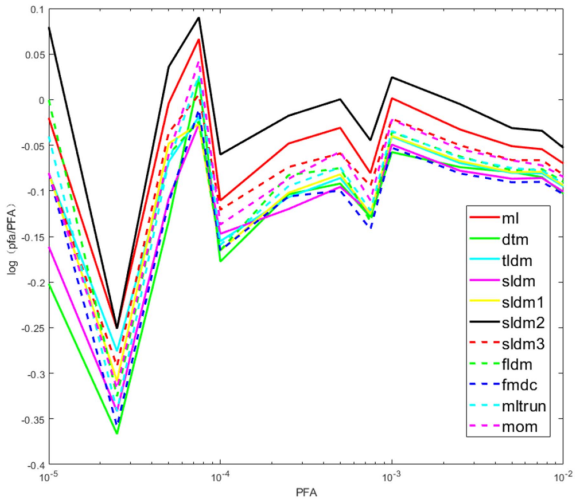

(b)

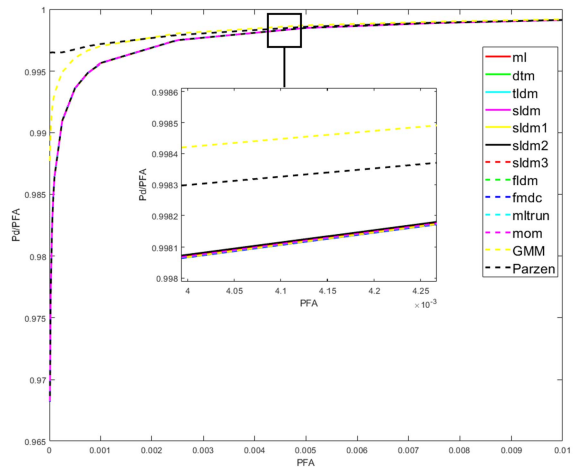

(c)

Fig. 6. CFAR performance. (a) C_L of GMM and Parzen window kernel method. (b) C_L of model-based method. (c) ROC of GMM, Parzen window kernel method and model-based methods.

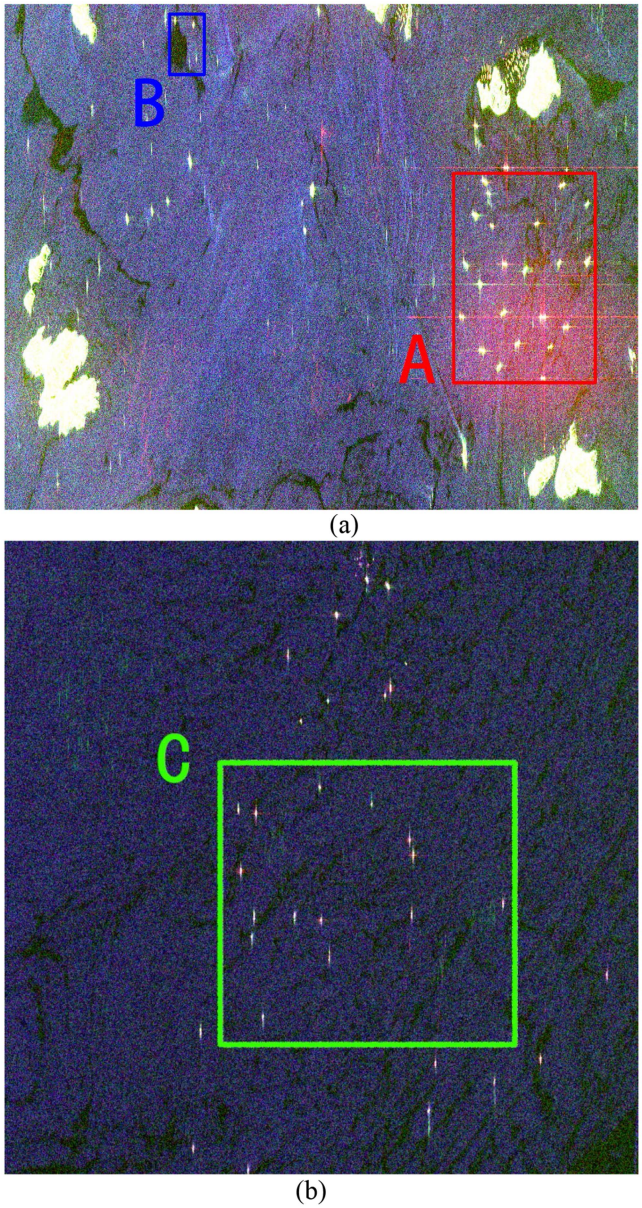

Fig. 7. Fully polarized SLC RADARSAT-2 SAR image. (a) Waters southwest to Lantau Island. (b) Waters northwest of Laizhou Bay.

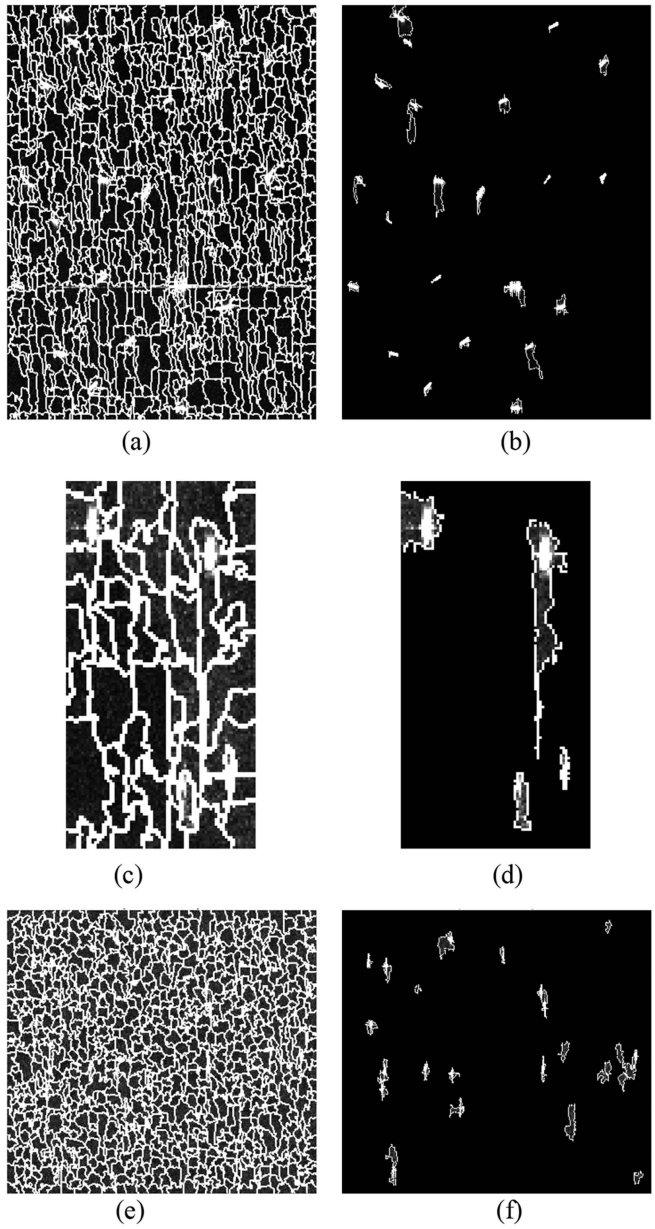

Fig. 8. Results of superpixel segmentation. (a) Superpixel segmentation (ROI A). (b) Candidate target (ROI A). (c) Superpixel segmentation (ROI B). (d) Candidate target (ROI B). (e) Superpixel segmentation (ROI C). (f) Candidate target (ROI C).

The total sample size is 100 000 and Monte Carlo simulation time is 1000. The truncation depth is set to $R_{t1} = 0.3$ and $R_{t2} = 0.2$ for achieving an accurate bilateral truncation. The CFAR performance of the learning-based and model-based method under the bilateral truncation situation is presented in Fig. 6.

As shown in Fig. 6(a), the maintenance of the false alarm rate of GMM and Parzen window kernel method is close to zero only when the false alarm rate comes to near 0.01. Fig. 6(b) shows that the model-based method with the ENL estimators mentioned above exhibits similar performance that the maintenance of the false alarm rate is almost zero, indicating that the model-based method under the condition of bilateral truncation is correct and efficient. Fig. 6(c) shows that GMM and Parzen window kernel methods share similar performance with model-based methods in the detection rate. Therefore, the GMM and Parzen window kernel method cannot achieve better CFAR performance than the model-based method when a low false rate alarm is required.

E. Real Data for Experiments

Two RADARSAT-2 fully polarimetric SLC SAR datasets are used to validate the performance of the superpixel-level BTS CFAR detector. One dataset was acquired on September 11, 2017, over the waters southwest of Lantau Island with a size of 1582×3154 pixels. Another image was acquired on September 23, 2015, over the waters northwest of Laizhou Bay with a size

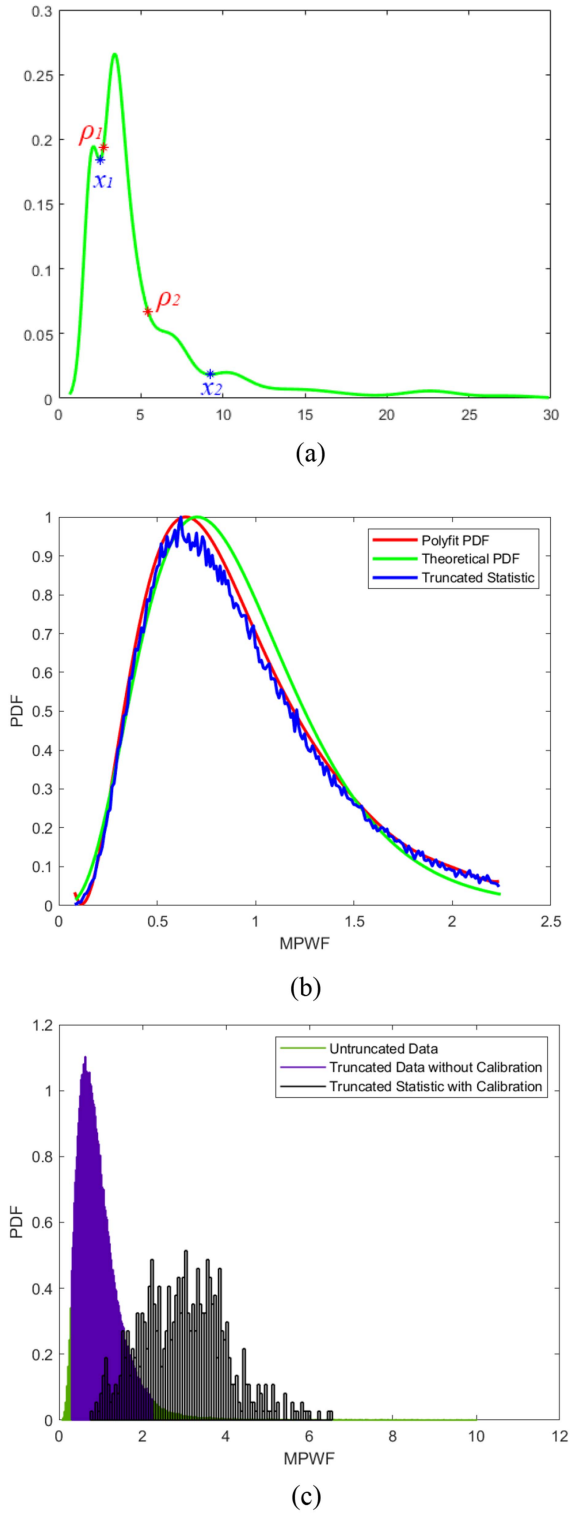

Fig. 9. Results of data truncation. (a) PDF of the untruncated data. (b) PDF of the truncated data. (c) Histogram of the data.

of 1894×3261 pixels. The resolution of both sets is 8×8 m. Region of interest (ROI) A, B, and C are shown in Fig. 7. A multilook process is used to reduce speckles, where the nominal number of looks is set as 4. The PFA in the experiments is set to 0.0001.

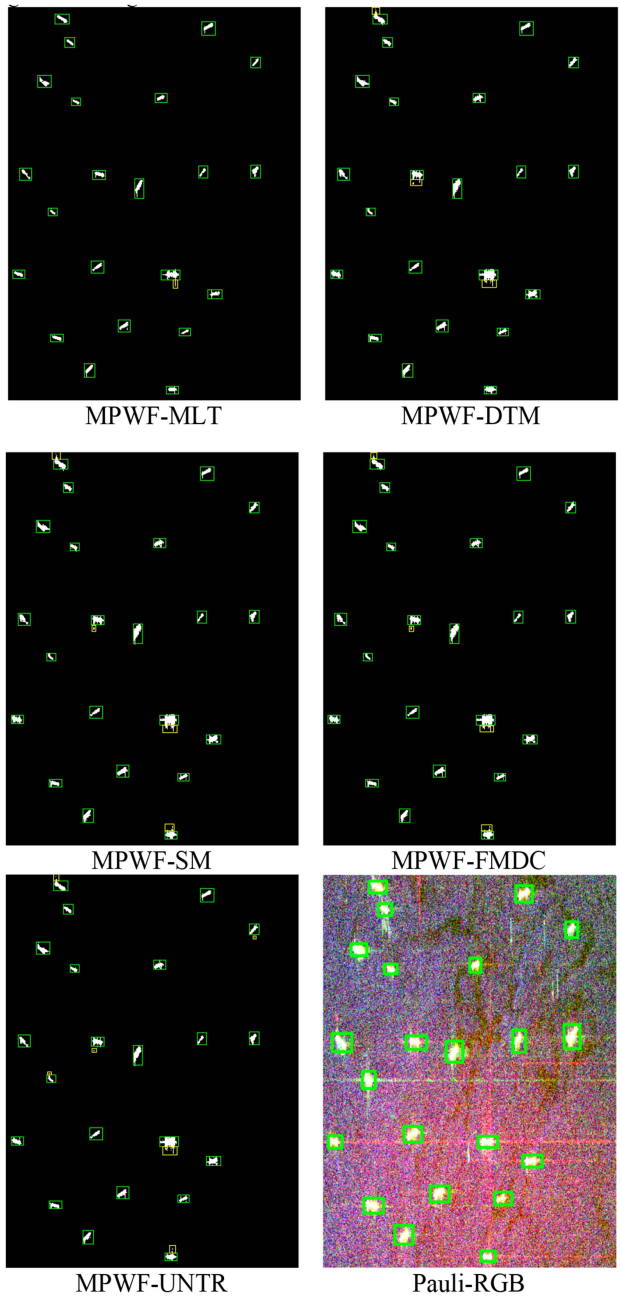

Fig. 10. Detection results of ROI A: MPWF-MLT, MPWF-DTM, MPWF-SM, MPWF-FMDC, MPWF-UNTR, and Pauli-RGB.

F. Results of Superpixel Segmentation

As described in the methodology, the superpixel segmentation is performed and the candidate target superpixels are selected. The results of superpixel segmentation are shown in Fig. 8. The segmentation results are presented in the left column and the candidate target superpixels are presented in the right column.

G. Data Truncation

As described in Section III-B, the truncation threshold is determined adaptively by (21). Observing the results presented in Figs. 4 and 5, it can be found that the over-truncation causes

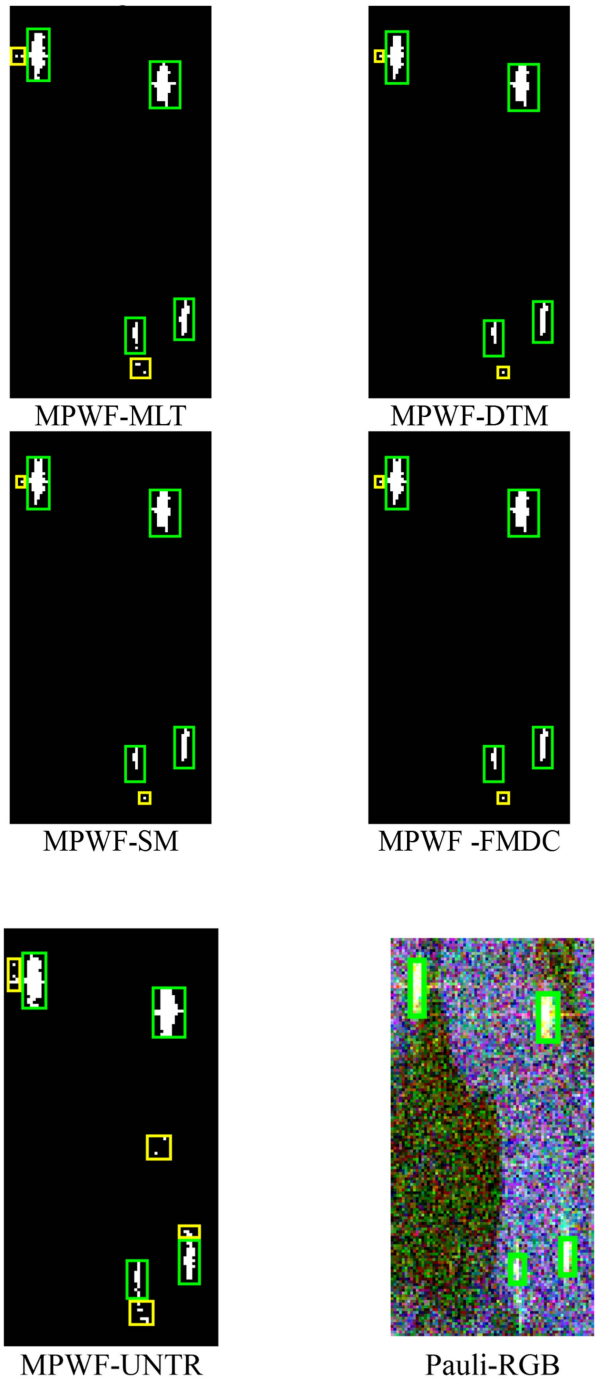

Fig. 11. Detection results of ROI B: MPWF-MLT, MPWF-DTM, MPWF-SM, MPWF–FMDC, MPWF-UNTR, and Pauli-RGB.

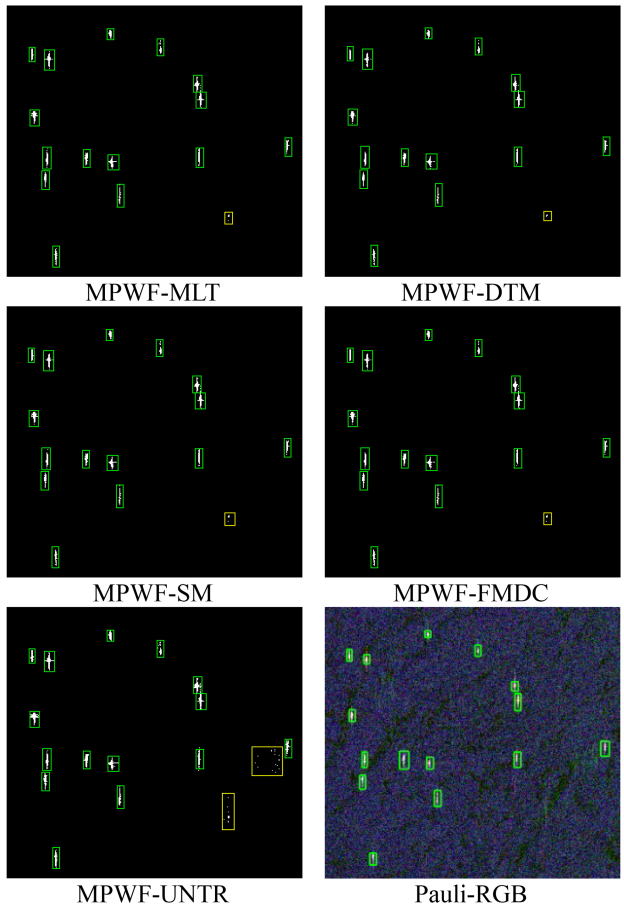

Fig. 12. Detection results of ROI C: MPWF-MLT, MPWF-DTM, MPWF-SM, MPWF-FMDC, MPWF-UNTR, and Pauli-RGB.

a slight degradation in the ENL estimation performance. However, appropriate over-truncation can also bring less difference between the PDF of the truncated data and the theoretical Gamma distribution PDF. Thus, for the most accurate estimation of the ENL, $\sum |Y_{\mathrm{GT}} - Y_{\mathrm{PDF}}|$ is multiplied by $\frac{N_T}{N_A}$ in (20). $\sum |Y_{\mathrm{GT}} - Y_{\mathrm{PDF}}|$ represents the difference between the PDF of the truncated data and the theoretical Gamma distribution PDF. $\frac{N_T}{N_A}$ represents the size of the truncated data. The minimum of (20) denotes the optimal combination of the truncated data size and the PDF fit degree. The truncation results of ROI A are shown in Fig. 9.

The PDF of the untruncated data is shown in Fig. 9(a) where the local minimum values of PDF are marked with blue $*$ and the bilateral truncation thresholds are with red $*$.

In Fig. 9(b), the PDF of the truncated data fitted by the poly function is represented by the red curve. The theoretical gamma distribution PDF is shown with the green curve. The histogram of the truncated data is shown with the blue curve. It can be observed that the PDF of the truncated data is very close to the theoretical PDF.

In Fig. 9(c), the histogram of the untruncated data is shown with green bars, the histogram of the truncated data without calibration is shown with purple bars, and the histogram of the truncated data without calibration via (14) is shown with black bars. From the result, it can be observed that the truncated data with calibration is centered at 3, consistent with the theoretical value, which indicates that the truncation is effective and the parameter estimation is accurate.

H. Detection Performance Analysis

The ENL estimators mentioned in Section III-C are used for parameter estimation, and the corresponding detection performance is presented in the following figures. We take sldm2

TABLE I
PERFORMANCES OF THE DETECTORS

Area	Method	$P_{fa}(10^{-4})$	N_{td}	N_{fa}	$FoM(\%)$
A	ENL-MLT	1.3840	1042	167	61.40
	ENL-DTM	5.1218	1191	618	55.45
	ENL-SM	5.8262	1196	703	53.56
	ENL-FMDC	5.6273	1194	679	54.05
	ENL- UNTR	4.1936	1179	506	57.91
Area	Method	$P_{fa}(10^{-4})$	N_{td}	N_{fa}	$FoM(\%)$
B	ENL-MLT	1.9801	95	55	54.29
	ENL-DTM	2.6641	100	74	51.55
	ENL-SM	2.1601	96	60	53.33
	ENL-FMDC	2.1601	96	60	53.33
	ENL- UNTR	4.7882	107	133	42.29
Area	Method	$P_{fa}(10^{-4})$	N_{td}	N_{fa}	$FoM(\%)$
C	ENL-MLT	0.9558	287	274	38.42
	ENL-DTM	0.7534	276	216	40.06
	ENL-SM	0.9069	284	260	38.74
	ENL-FMDC	0.8546	281	245	39.14
	ENL- UNTR	1.3464	316	386	36.79

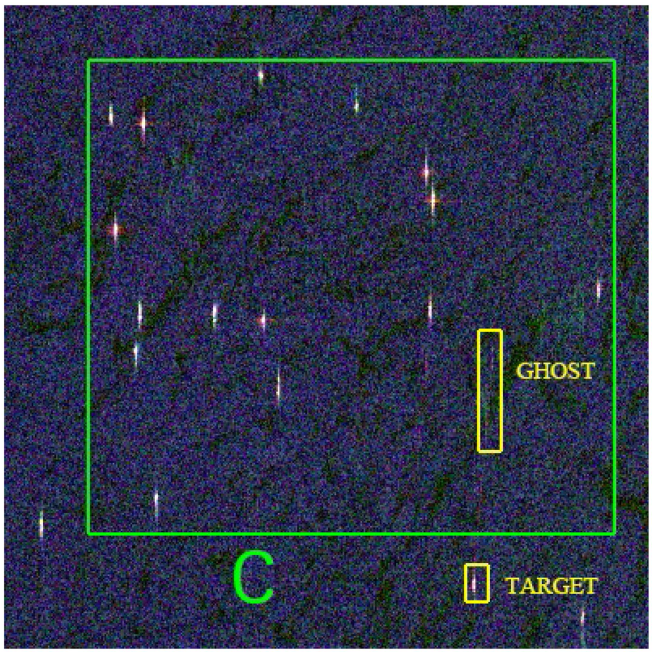

Fig. 13. Target causing the false alarm in ROI C.

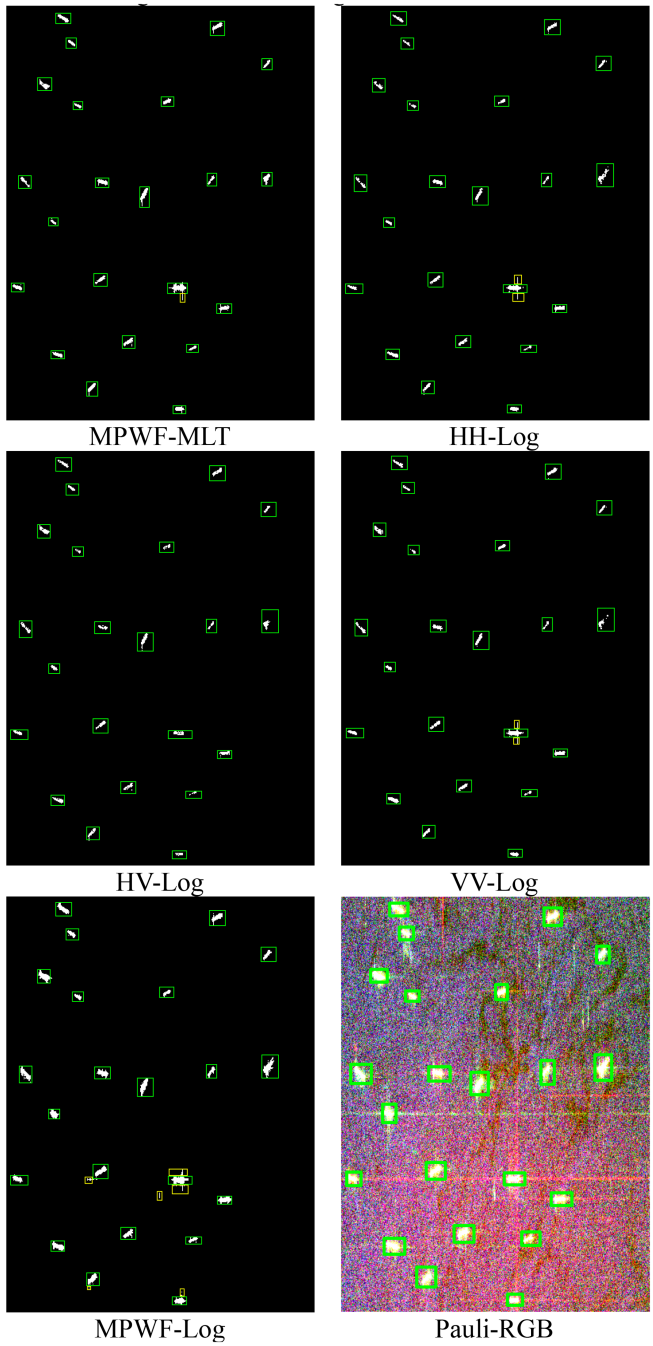

Fig. 14. Detection results of ROI A: MPWF-MLT, HH-Log, HV-Log, VV-Log, MPWF-Log, and Pauli-RGB.

as the ENL-SM method. MPWF-xxx means that the detection is performed using the ENL-xxx estimator. MPWF-UNTR involves performing detection without bilateral truncation. Based on the CFAR results, DBSCAN is used for false alarm rejection with eps $= 20$ and MinPt $= 2$ [38]. The detection results are presented in Figs. 10–12 and Table I. The ground truth is given as ma Pauli-RGB image. The omitted target is marked with a red rectangle, the false target is marked with a yellow rectangle, and the true target is marked with a green rectangle.

In addition, a figure of merit (FoM) [39] is used to evaluate the detection performance as follows:

$$\text{FoM} = \frac{N_{td}}{N_{fa} + N_{gt}} \tag{32}$$

where N_{td} is the number of detected ships, N_{fa} is the number of false ships, and N_{gt} is the number of real ships in the ROI.

From the result, observe that all methods detect the targets with no omittance, which validates that the proposed superpixel-level polarimetric BTS CFAR detector can efficiently detect

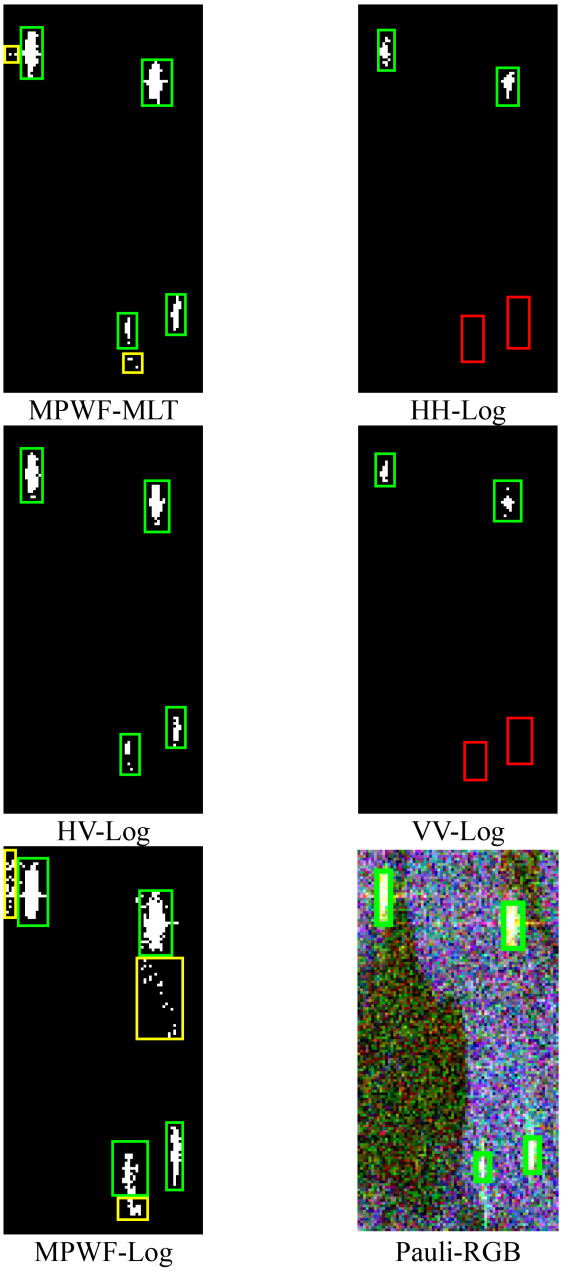

Fig. 15. Detection results of ROI B: MPWF-MLT, HH-Log, HV-Log, VV-Log, MPWF-Log, and Pauli-RGB.

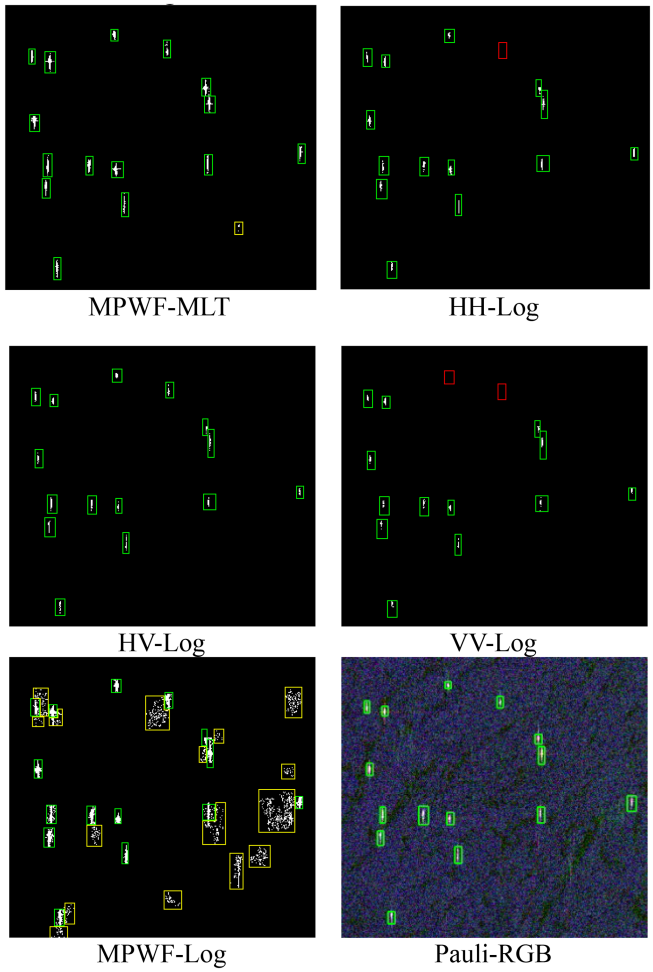

Fig. 16. Detection results of ROI C: MPWF-MLT, HH-Log, HV-Log, VV-Log, MPWF-Log, and Pauli-RGB.

targets from background clutter. Among the ENL estimators compared, ENL-UNTR produces the greatest number of false alarms, from which the necessity and contribution of truncation can be verified. The ENL-SM and ENL-FMDC share similar performance in both the false alarm rate maintenance and the detection rate followed by ENL-DTM. The ENL-MLT method provides the best performance in terms of both false alarm rate maintenance and detection rate.

Notice from the results that the ship side lobe and the azimuth ambiguity significantly degrade the detection performance, which can be obviously observed in the yellow rectangles in ROI C. The false alarm is caused by the ghost (azimuth ambiguity) of the target near ROI C presented in Fig. 13 with the yellow rectangle. In ROI A and ROI B, it also can be observed that the detection results are expanded by several pixels. The azimuth ambiguity elimination and the sidelobe suppression are the next problems to be addressed.

I. Compared With Log-Normal Distribution

The method proposed in this study is compared with the CFAR detector using HH, HV, VV, and MPWF under log-normal distribution. The detection performance is presented in Figs. 14–16. The ground truth is given as the Pauli-RGB image. We take the method proposed in this study as MPWF-MLT and xx-Log means the CFAR detector using xx value under log-normal distribution.

From the results, observe that the method proposed in this study performs best. The detectors based on HH and VV channels under log-normal distribution cause the most omittance. Although the detectors utilizing the HV channel cost less omittance, the detail and edge information of the detected ship targets are missing. Since the bias of the distribution modeling, the MPWF-log detector causes most false alarms and performs poorly in false alarm maintenance.

V. Conclusion

In this study, a novel CFAR detector for PolSAR data based on superpixel segmentation and elliptical truncation is proposed. The proposed method utilizes the similarity between the MPWF and truncation constraint in [25] to introduce bilateral truncation into MPWF data processing. The relationship between the moments before and after the truncation is derived.

The superpixel segmentation is utilized as a preprocessing on the MPWF data characterizing the clutter close to the target. The MLE estimator of the ENL is derived and compared with other estimators. An adaptive bilateral truncation method is designed according to the analysis of the influence of the truncation depth and the comparison between the learning-based and the model-based methods. It is validated that the MLE estimator gives the best performance in both the false alarm rate maintenance and the detection rate under the proposed method via the experiments based on the simulated and measured data from RADARSAT-2.

The experimental results demonstrate that the superpixel-level polarimetric BTS CFAR detector leads to a good detection performance in the case that outliers exist. However, the detection performance can be affected greatly by the sidelobe and the azimuth ambiguity, that is ghosting. Ghost elimination and sidelobe suppression are the next problems to be addressed.

Appendix

The scattering vector $\mathbf{k}$ follows the d-dimensional multinormal distribution as stated in the following equation:

$$p(\mathbf{k}) = \frac{1}{\pi^d |\mathbf{\Sigma}|} \exp(-\mathbf{k}^\dagger \mathbf{\Sigma}^{-1} \mathbf{k}) \tag{33}$$

where d is the dimension of $\mathbf{k}$ and $\mathbf{\Sigma}$ is the SM of the multilook covariance matrix $\mathbf{C}$.

The MPWF for L looks can be obtained from the following expression:

$$z = \frac{1}{L} \sum_{i=1}^{L} \mathbf{k}_i^\dagger \mathbf{\Sigma}^{-1} \mathbf{k}_i = \mathrm{tr}(\mathbf{\Sigma}^{-1} \mathbf{C}). \tag{34}$$

The truncation constraint reported in [25] is expressed as follows:

$$E = \{\mathbf{x} | a \le \mathbf{x}' \mathbf{R}^{-1} \mathbf{x} \le b\}, 0 \le a \le b \tag{35}$$

where $\mathbf{x}$ is a multivariate vector and $'$ is the transpose operator.

Coincidentally, the constraint shares a form similar to that expressed in (34) when $L = 1$. Thus, the truncation set $\mathfrak{D}$ can be defined as follows:

$$\mathfrak{D} = \left\{ \mathbf{k} \left| L\rho_1 \le \sum_{i=1}^{L} \mathbf{k}^\dagger \mathbf{\Sigma}^{-1} \mathbf{k}_i = L\mathrm{tr}\left(\mathbf{\Sigma}^{-1} \mathbf{C}\right) \le L\rho_2 \right. \right\} \tag{36}$$

where ρ_1 is the lower truncation threshold and ρ_2 is the higher truncation threshold.

Because $\mathbf{k}$ is a complex vector, we expend it to a real vector $\mathbf{r}$ having 2-D dimension as follows:

$$\mathbf{r} = \begin{bmatrix} S_{HH}^r & \sqrt{2} S_{\mathrm{HV}}^r & S_{\mathrm{VV}}^r & S_{\mathrm{HH}}^i & \sqrt{2} S_{\mathrm{HV}}^i & S_{\mathrm{VV}}^i \end{bmatrix}^T \tag{37}$$

where the superscripts r and i denote the real and imaginary parts of the element, respectively, and T denotes the transpose. Then, the PDF of $\mathbf{r}$ can be expressed as follows:

$$p(\mathbf{r}) = (2\pi)^{-d} |\mathbf{R}|^{-\frac{1}{2}} \exp\left(-\frac{1}{2} \mathbf{r}' \mathbf{R}^{-1} \mathbf{r}\right) \tag{38}$$

where $\mathbf{R} = \begin{bmatrix} \frac{1}{2}\mathbf{\Sigma} & \mathbf{0} \\ \mathbf{0} & \frac{1}{2}\mathbf{\Sigma} \end{bmatrix}$. The joint PDF of L independent samples based on (37) should be expressed as follows:

$$p(\mathbf{r}_1, \mathbf{r}_2, \ldots, \mathbf{r}_L) = (2\pi)^{-Ld} |\mathbf{R}|^{-\frac{L}{2}} \exp\left(-\frac{1}{2} \sum_{i=1}^{L} \mathbf{r}_i' \mathbf{R}^{-1} \mathbf{r}_i\right). \tag{39}$$

We can denote $\mathbf{y} = (\mathbf{r}_1, \mathbf{r}_2, \ldots, \mathbf{r}_L)$ and then (39) yields the following:

$$p(\mathbf{y}) = (2\pi)^{-Ld} |\mathbf{\Xi}|^{-\frac{1}{2}} \exp\left(-\frac{1}{2} \mathbf{y}' \mathbf{\Xi}^{-1} \mathbf{y}\right) \tag{40}$$

where $\mathbf{\Xi} = \begin{bmatrix} \frac{1}{2}\mathbf{\Sigma} & 0 & \ldots & 0 \\ 0 & \frac{1}{2}\mathbf{\Sigma} & \ddots & 0 \\ \vdots & \ddots & \ddots & \vdots \\ 0 & 0 & \ldots & \frac{1}{2}\mathbf{\Sigma} \end{bmatrix}$.

Evidently, (40) shares the same form as (12). The differences between them lie in their dimensions. Therefore, the following equations are satisfied:

$$\mathbf{\Xi} = \mu(\rho_1, \rho_2) \Theta(\rho_1, \rho_2; \mathbf{\Sigma}) \tag{41}$$

$$\mu(\rho_1, \rho_2) \equiv \frac{F_{2Ld}(L\rho_2) - F_{2Ld}(L\rho_1)}{F_{2Ld+2}(L\rho_2) - F_{2Ld+2}(L\rho_2)} \tag{42}$$

where $\Theta(\rho_1, \rho_2; \mathbf{\Sigma})$ denotes the second moment of the truncated data.

Because $\mathbf{\Xi}$ is a block diagonal matrix, defined as follows:

$$\mathbf{\Sigma} = \mu(\rho_1, \rho_2) \mathfrak{S}(\rho_1, \rho_2; \mathbf{\Sigma}) \tag{43}$$

$$\mu(\rho_1, \rho_2) \equiv \frac{F_{2Ld}(L\rho_2) - F_{2Ld}(L\rho_1)}{F_{2Ld+2}(L\rho_2) - F_{2Ld+2}(L\rho_2)} \tag{44}$$

where $\mathfrak{S}(\rho_1, \rho_2; \mathbf{\Sigma})$ denotes the second moment of the truncated data.

References

[1] A. Marino, S. R. Cloude, and I. H. Woodhouse, "Detecting depolarized targets using a new geometrical perturbation filter," *IEEE Trans. Geosci. Remote Sens.*, vol. 50, no. 10, pp. 3787–3799, Oct. 2012.

[2] L. M. Novak, M. B. Sechtin, and M. J. Cardullo, "Studies of target detection algorithms that use polarimetric radar data," *IEEE Trans. Aerosp. Electron. Syst.*, vol. 25, no. 2, pp. 150–165, Mar. 1989.

[3] T. Liu, Z. Yang, A. Marino, G. Gao, and J. Yang, "Joint polarimetric subspace detector based on modified linear discriminant analysis," *IEEE Trans. Geosci. Remote Sens.*, vol. 60, 2022, Art. no. 5223519, doi: 10.1109/TGRS.2022.3148979.

[4] L. M. Novak and M. C. Burl, "Optimal speckle reduction in polarimetric SAR imagery," *IEEE Trans. Aerosp. Electron. Syst.*, vol. 26, no. 2, pp. 293–305, Mar. 1990.

[5] L. M. Novak et al., "Optimal polarimetric processing for enhanced target detection," in *Proc. Telesyst. Conf.*, Oct. 1991, pp. 69–75.

[6] A. Lopes and F. Sery, "Optimal speckle reduction for the product model in multilook polarimetric SAR imagery and the wishart distribution," *IEEE Trans. Geosci. Remote Sens.*, vol. 35, no. 3, pp. 632–647, May 1997.

[7] G. Liu, S. Huang, A. Torre, and F. Rubertone, "The multilook polarimetric whitening filter (MPWF) for intensity speckle reduction in polarimetric SAR images," *IEEE Trans. Geosci. Remote Sens.*, vol. 36, no. 3, pp. 1016–1020, May 1998.
[8] T. Liu, J. Zhang, G. Gao, J. Yang, and A. Marino, "CFAR ship detection in polarimetric synthetic aperture radar images based on whitening filter," *IEEE Trans. Geosci. Remote Sens.*, vol. 58, no. 1, pp. 58–81, Jan. 2020, doi: 10.1109/TGRS.2019.2931353.
[9] A. Marino, "A notch filter for ship detection with polarimetric SAR data," *IEEE J. Sel. Topics Appl. Earth Observ. Remote Sens.*, vol. 6, no. 3, pp. 1219–1232, Jun. 2013.
[10] A. Marino, M. Sugimoto, K. Ouchi, and I. Hajnsek, "Validating a notch filter for detection of targets at sea with ALOS-PALSAR data: Tokyo bay," *IEEE J. Sel. Topics Appl. Earth Observ. Remote Sens.*, vol. 7, no. 12, pp. 4907–4918, Dec. 2014.
[11] T. Liu, Z. Yang, T. Zhang, Y. Du, and A. Marino, "A new form of the polarimetric notch filter," *IEEE Geosci. Remote Sens. Lett.*, vol. 19, 2020, Art. no. 4001405, doi: 10.1109/LGRS.2020.3020052.
[12] G. Gao and G. Shi, "CFAR ship detection in nonhomogeneous sea clutter using polarimetric SAR data based on the notch filter," *IEEE Trans. Geosci. Remote Sens.*, vol. 55, no. 8, pp. 4811–4824, Aug. 2017.
[13] M. Barkat, S. D. Himonas, and P. K. Varshney, "CFAR detection for multiple target situations," *Proc. IEE Proc. F*, vol. 136, no. 5, pp. 193–209, 1989.
[14] H. M. Finn and R. S. Johnson, "Adaptive detection mode with threshold control as a function of spatially sampled clutter-level estimates," *RCA Rev.*, vol. 29, pp. 414–464, Sep. 1968.
[15] V. G. Hansen and J. H. Sawyers, "Detectability loss due to 'greatest of' selection in a cell-averaging CFAR," *IEEE Trans. Aerosp. Electron. Syst.*, vol. AES-16, no. 1, pp. 115–118, Jan. 1980.
[16] G. V. Trunk, "Range resolution of targets using automatic detectors," *IEEE Trans. Aerosp. Electron. Syst.*, vol. AES-14, no. 5, pp. 750–755, Sep. 1978.
[17] M. E. Smith and P. K. Varshney, "Intelligent CFAR processor based on data variability," *IEEE Trans. Aerosp. Electron. Syst.*, vol. 36, no. 3, pp. 837–847, Jul. 2000.
[18] H. Rohling, "Radar CFAR thresholding in clutter and multiple target situations," *IEEE Trans. Aerosp. Electron. Syst.*, vol. AES-19, no. 4, pp. 608–621, Jul. 1983.
[19] P. Gandhi and S. Kassam, "Analysis of CFAR processors in nonhomogeneous background," *IEEE Trans. Aerosp. Electron. Syst.*, vol. AES-24, no. 4, pp. 427–445, Jul. 1988.
[20] D. Tao, S. N. Anfinsen, and C. Brekke, "Robust CFAR detector based on truncated statistics in multiple-target situations," *IEEE Trans. Geosci. Remote Sens.*, vol. 54, no. 1, pp. 117–134, Jan. 2016.
[21] D. Tao, A. P. Doulgeris, and C. Brekke, "A segmentation-based CFAR detection algorithm using truncated statistics," *IEEE Trans. Geosci. Remote Sens.*, vol. 54, no. 5, pp. 2887–2898, May 2016.
[22] J. Zhou, J. Xie, X. Liao, and C. Sun, "Robust sliding window CFAR detection based on quantile truncated statistics," *IEEE Trans. Geosci. Remote Sens.*, vol. 60, 2022, Art. no. 5117823.
[23] J. Ai et al., "Robust CFAR ship detector based on bilateral-trimmed-statistics of complex ocean scenes in SAR imagery: A closed-form solution," *IEEE Trans. Aerosp. Electron. Syst.*, vol. 57, no. 3, pp. 1872–1890, Jun. 2021.
[24] T. Liu, Z. Yang, A. Marino, G. Gao, and J. Yang, "Robust CFAR detector based on truncated statistics for polarimetric synthetic aperture radar," *IEEE Trans. Geosci. Remote Sens.*, vol. 58, no. 9, pp. 6731–6747, Sep. 2020, doi: 10.1109/TGRS.2020.2979252.
[25] G. M. Tallis, "Elliptical and radial truncation in normal populations," *Ann. Math. Statist.*, vol. 34, no. 3, pp. 940–944, Sep. 1963. [Online]. Available: https://www.jstor.org/stable/2238475
[26] S. N. Anfinsen, A. P. Doulgeris, and T. Eltoft, "Estimation of the equivalent number of looks in polarimetric synthetic aperture radar imagery," *IEEE Trans. Geosci. Remote Sens.*, vol. 47, no. 11, pp. 3795–3809, Nov. 2009.
[27] L. Tao, C. Hao-Gui, X. Ze-min, and G. Jun, "Texture-invariant estimation of equivalent number of looks based on trace moments in polarimetric radar imagery," *IEEE Geosci Remote Sens Lett.*, vol. 11, no. 6, pp. 1129–1133, Jun. 2014.
[28] T. Liu, H. Cui, Z. Xi, and J. Gao, "Novel estimators of equivalent number of looks in polarimetric SAR imagery based on sub-matrices," *Sci. China Inf. Sci.*, vol. 59, no. 6, Jun. 2016, Art. no. 062309, doi: 10.1007/s11432-015-5480-x.
[29] N. Bouhlel, "Parameter estimation of multilook polarimetric SAR data based on fractional determinant moments," *IEEE Geosci. Remote Sens. Lett.*, vol. 16, no. 7, pp. 1075–1079, Jul. 2019.
[30] A. P. Doulgeris, S. N. Anfinsen, and T. Eltoft, "Automated non-Gaussian clustering of polarimetric synthetic aperture radar images," *IEEE Trans. Geosci. Remote Sens.*, vol. 49, no. 10, pp. 3665–3676, Oct. 2011.
[31] Y. Wang and H. Liu, "PolSAR ship detection based on superpixel-level scattering mechanism distribution features," *IEEE Geosci. Remote Sens. Lett.*, vol. 12, no. 8, pp. 1780–1784, Aug. 2015.
[32] M.-D. Li, X.-C. Cui, and S.-W. Chen, "Adaptive superpixel-level CFAR detector for SAR inshore dense ship detection," *IEEE Geosci. Remote Sens. Lett.*, vol. 19, 2022, Art. no. 4010405.
[33] G. Gao, "A Parzen-window-kernel-based CFAR algorithm for ship detection in SAR images," *IEEE Geosci. Remote Sens. Lett.*, vol. 8, no. 3, pp. 557–561, May 2011, doi: 10.1109/LGRS.2010.2090492.
[34] T. Liu, Z. Yang, G. Gao, A. Marino, S. W. Chen, and J. Yang, "A general framework of polarimetric detectors based on quadratic optimization," *IEEE Trans. Geosci. Remote Sens.*, vol. 60, 2022, Art. no. 5237418, doi: 10.1109/TGRS.2022.3217336.
[35] A. Lopes and F. Sery, "Optimal speckle reduction for the product model in multilook polarimetric SAR imagery and the wishart distribution," *IEEE Trans. Geosci. Remote Sens.*, vol. 35, no. 3, pp. 632–647, May 1997.
[36] S. Khan and R. Guida, "On fractional moments of multilook polarimetric whitening filter for polarimetric SAR data," *IEEE Trans. Geosci. Remote Sens.*, vol. 52, no. 6, pp. 3502–3512, Jun. 2014.
[37] T. Li, Z. Liu, R. Xie, and L. Ran, "An improved superpixel-level CFAR detection method for ship targets in high-resolution SAR images," *IEEE J. Sel. Topics Appl. Earth Observ. Remote Sens.*, vol. 11, no. 1, pp. 184–194, Jan. 2018.
[38] M. Ester, H.-P. Kriegel, J. Sander, and X. Xu, "A density-based algorithm for discovering clusters in large spatial databases with noise," in *Proc. 2nd Int. Conf. Knowl. Discov. Data Mining*, Aug. 1996, pp. 1–6.
[39] R. L. Paes, J. A. Lorenzzetti, and D. F. M. Gherardi, "Ship detection using TerraSAR-X images in the Campos Basin (Brazil)," *IEEE Geosci. Remote Sens. Lett.*, vol. 7, no. 3, pp. 545–548, Jul. 2010.
[40] J. Wishart, "The generalised product moment distribution in samples from a normal multivariate population," *Biometrika*, vol. 20A, no. 1/2, pp. 32–52, 1928.
[41] N. R. Goodman, "Statistical analysis based on a certain multivariate complex Gaussian distribution (an introduction)," *Ann. Math. Statist.*, vol. 34, no. 1, pp. 152–177, Mar. 1963.
[42] M. Abramowitz and I. A. Stegun, *Handbook of Mathematical Functions With Formulas, Graphs, and Mathematical Tables*. New York, NY, USA: Dover, 2001.

Wenxing Mu received the B.S. degree in radar engineering from the Naval University of Engineering (NUE), Wuhan, China, in 2020. He is currently working toward the Ph.D. degree in information and communication engineering with the Naval University of Engineering, Wuhan, China.

His research interests include radar polarization information process and electronic warfare system modeling and SAR ground moving target indication.

Ning Wang received the B.S. degree in communication engineering from the Jiangsu University of Science and Technology, Zhenjiang, China, in 2017, and the M.S. degree in electronic information in 2022 from the Naval Engineering University, Wuhan, China, where she is currently working toward the Ph.D. degree in information and communication engineering.

Her research interests include synthetic aperture radar target recognition and detection.

Lu Fang received the B.S. degree in electronic and information engineering and the M.S. degree in electronic and communication engineering from Yantai University, Yantai, China, in 2016 and 2019, respectively. She is currently working toward the Ph.D. degree in information and communication engineering with the Naval University of Engineering, Wuhan, China.

Tao Liu received the B.S. degree in communication engineering and the Ph.D. degree in information and communication engineering from the National University of Defense Technology, Changsha, China, in 2001 and 2007, respectively.

In 2000, he was the Outstanding Communist Youth League member of China. Since 2007, he has been a Professor with the School of Electronic Engineering, Naval University of Engineering, Wuhan, China. He authored more than 50 journal papers and three books. His research interests include the statistical theory of radar polarization, polarization information processing, synthetic aperture radar (SAR) automatic target recognition, statistical modeling of SAR images, SAR ship detection, interferometric SAR, SAR ground moving target indication, and artificial intelligence.

Dr. Liu has been a committee member with the Radar Branch of the Chinese Institute of Electronics since 2019. In 2009, he was the recipient of the Award of Excellent Doctor Thesis of the Chinese Army.